Impact Modified Isotatic Polypropylene with Controlled Rubber Intrinsic Viscosities: Some New Aspects About Morphology and Fracture

C. Grein, K. Bernreitner, A. Hauer, M. Gahleitner, W. Neißl

Borealis GmbH, St.-Peter Straße 25, A-4021 Linz, Austria

ABSTRACT: The influence of the molecular weight of the dispersed phase of ethylene–propylene rubber modified isotactic polypropylene (iPP/EPR) reactor blends was studied in a systematic way by varying their intrinsic viscosity (IV) from 1.7 to 6 dg/L while keeping the matrix melt flow rate (MFR) constant. Standard Charpy measurements were completed by a continuous analysis of the impact properties over a wide range of temperatures at fixed test speed. As expected, the higher the IV, the tougher the iPP/EPR blends. However, ductile–brittle transitions as key mechanical descriptors did not correlate linearly with M_w, suggesting the macroscopic behavior of the blend to be controlled primarily by the morphology of the EPR particles. Moreover, strong correlations were found between impact mechanical properties, amount of stress-whitening, and strength of the molecular relaxations estimated from dynamical mechanical analysis. © 2002 Wiley Periodicals, Inc. J Appl Polym Sci 87: 1702–1712, 2003

Key words: ethylene–propylene rubber modified isotactic polypropylene blends; intrinsic viscosity; fracture; ductile–brittle transition; morphology; dynamic mechanical analysis;

INTRODUCTION

The attractiveness of isotactic polypropylene (iPP) is related to its excellent cost-to-performance ratio. Its brittleness at high speed or low temperature, however, limits its utilization as engineering thermoplastic. Impact modifiers such as ethylene–propylene–diene copolymer (EPDM) or ethylene–propylene copolymer (EPR) are therefore often added to iPP, either directly in the reactor or in compounding step, in order to improve its toughness.[1–5] End-use performances of those heterogeneous systems result from synergies between matrix and dispersed phase: neat iPP dissipates the energy in the form of shearing or craze formation, while the particles, acting as stress concentrators, create the conditions to make it possible. The most important factors to control the impact properties of such blends were shown to be (1) the molecular weight, molecular weight distribution, and crystallinity of the matrix; (2) the particle size, volume fraction, molecular weight, and ethylene content of the rubber; and (3) the compatibility of both phases.[6–15] Their respective influence is briefly outlined here.

An iPP with high molecular weight is beneficial for the energy of homopolymers and copolymers to break because of increased inter- and intralamellar link density (i.e., higher amount of entanglements and tie molecules), which promotes shear yielding rather than multiple or single crazing.[7,9,16–20] The effect of crystallinity, X_c, is more controversial, detrimental or positive effects having been reported.[21,22] Karger–Kocsis proposed that the toughness goes through a maximum vs X_c as a consequence of the competition between lamellar buildup, which leads to thicker and more perfect crystallites with increasing X_c, and tie-molecule density, which decreases with increasing X_c. An increasing concentration of elastomer particles improves the impact properties of rubber modified iPP, since they constitute nucleation sites for plasticity.[1,2,8,10,11,23–27] However, the volume fraction of EPR does not exceed 25–30 wt % in practice, the associated reduction of stiffness being undesirable for commercial applications. Keeping the rubber content constant at a level of about 20–30 wt %, optimum mechanical performances, in both static and dynamic tests conditions, were correlated with an optimum rubber particle size. The latter was shown to be stress state and temperature dependent, being about 400–600 nm at 23°C, 800–1000 nm at 0°C, and 1200–1500 nm at −40°C.[8,12,14,28–30] Shear yielding was therefore suggested to be the prevalent deformation mode at room temperature (even at relatively high speeds), whereas crazing was claimed to be the predominant one at $T < T_g$ (i.e., $T < 0°C$). Finally, a concentration of 40–50 mol % ethylene in the rubber has been reported to give

the best mechanical performances.[5,14] The particles are then immiscible enough with the matrix to maintain the desired phase separation, but sufficiently miscible with iPP to obtain a good compatibility between both phases.

The influence of the MFR of the particles, however, has been less documented, although it has been established that the molecular weights of the EPR and the matrix determine primarily the phase structure and the strength of the two phases. The aim of this study was to evaluate the morphological evolution and mechanical performance of iPP/EPR blends with various particle intrinsic viscosities while keeping the melt flow rate (MFR) of the matrix and the rubber fraction constant. Correlations between the structure and the properties of these blends were achieved by use of conventional Charpy tests, determination of the ductile–brittle transition of selected grades, and transmission electron micrographs.

EXPERIMENTAL

Materials

Seven model iPP/EPR reactor blends were studied. They are research material made in Borealis' pilot plant. The materials were produced in a liquid bulk polymerization process using a commercial fourth-generation catalyst with outside donor for isotacticity control. They were stabilized in order to prevent oxydation or any other form of degradation with a standard additive package after the reactor stage and during the pelletization stage. This latter was performed on a twin screw extruder (PRISM TSE 16 TC, 250 rotations per minute, $T = 210–220°C$). The nomenclature, which is used in this paper to describe them, was built as follows: iPP/EPR-IV = M-IV (i.e., M-1.7 for an intrinsic viscosity of 1.7 dL/g).

A summary of the main characteristics of the investigated grades is presented in Table I. Their matrix MFR was close to 40 g/10 min (ISO 1133, 230°C/2.16 kg), their EPR content roughly reflected by their xylene cold soluble value (XCS) was of about 23 wt %. While their monomer ratio (C_2: ethylene; C_3: propylene) during the EPR polymerization stage was kept

constant, the IV of the rubbery phase ranged from 1.7 to 6.0 dL/g. The IV were measured according to ISO 1628-1 at 135°C using decaline as solvent. The MFR of the blends decreased from 26 to 10 g/10 min with increasing IV of the particles. Gel permeation chromatography (GPC) was performed on a Waters 150 C at 135°C in trichlorobenzene. Whereas the M_n (respectively, M_w) of the matrix were constant, those of the particles (measured from the XCS fractions), increased from 56,000 to 180,000 (respectively, 233,000 to 1,2000,000) as expected from their IV. The molecular weight distributions (MWD) increased from about 4 to 6.7 with increasing IV.

Melting behavior and overall crystallinity were determined in differential scanning calorimetry (DSC) (TA 512 C, DIN 53765) in the second heat of the heat/cool/heat cycle between 23 and 250°C at 10 K/min. The degree of crystallinity was about $44 \pm 2\%$ for all materials, taking 207 J/g as melt enthalpy of a 100% crystalline iPP; the melt temperature of the iPP matrix was about 162°C.

Dynamic mechanical analysis (DMA) was performed on $10 \times 4 \times 1$ mm^3 compression molded bars from temperature scans between -140 and 140°C at 1 Hz using a Myrenne ATM3 torsion pendulum.

Microscopy

Polarized light microscopy was performed on 5 μm thick cuts of the injection molded specimens using a Olympus BX50. All the grades exhibited a classical skin–core morphology, but no differences could be found either in the size of the skin (150 μm) or in the distribution and size of the spherulites (2–5 μm). The fine morphology of the materials was observed either by transmission electron microscopy (TEM) (Philips CM-20) on 80 nm thin cuts at acceleration voltages of 100 kV or by scanning electron microscopy (Zeiss DSM 982 Gemini field emission) on ultrapolished surfaces at acceleration voltages between 2 and 10 kV. Samples were previously stained in an aqueous solution of ruthenium tetroxyde (RuO_4). Since contrast is provided by diffusion of RuO_4 into the specimen, the dark parts in Figure 1 represent an amorphous phase,

TABLE I
Main Characteristics of the Studied Materials

	MFR Total (g/10 min)	MFR Matrix (g/10 min)	IV (XCS) (dL/g)	XCS (%)	M_n (XCS) (g/mol)	M_w (XCS) (g/mol)	MWD (XCS) (−)
M-1.7	24	≈40	1.7	23.1	56,000	233,000	4.2
M-2.1	19.6	≈40	2.1	22.8	84,000	320,000	3.8
M-2.7	17.4	≈40	2.7	22.6	93,000	412,000	4.4
M-3.0	15.3	≈40	3	21.5	102,000	530,000	5.2
M-3.9	12.8	≈40	3.9	21.4	128,000	706,000	5.5
M-4.7	11.9	≈40	4.7	22.1	112,000	745,000	6.7
M-6.0	9.8	≈40	6	22.0	180,000	200,000	6.7
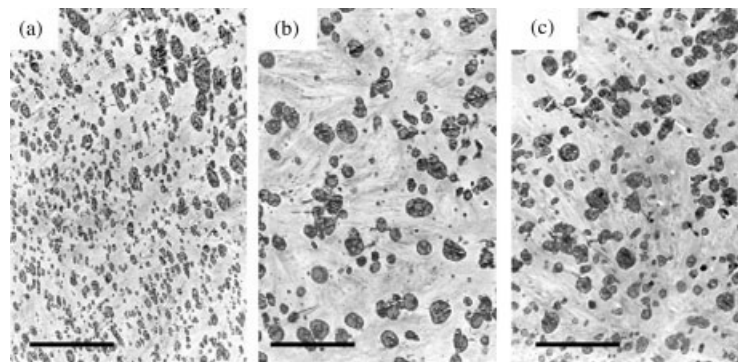
Figure 1 TEM micrographs of M-1.7, M-3, and M-6. The observed surface was perpendicular to flow direction. The scale represents 3 μm.

whereas the bright ones account for a crystalline phase. All the grades contained particles with an EPR/PE core–shell (single PE inclusion, typical for small particles) or "salami-like" (multiple PE inclusion, typical for big particles) structure.

The average particle diameters in number, D_n, in weight, D_w, and in volume, D_v, were evaluated with an image analyzer software (ProImage) on digitalized TEM micrographs without stereographic correction according to [31,32]:

$$D_n = \frac{\sum\limits_{i=1}^{N} n_i D_i}{\sum\limits_{i=1}^{N} n_i} \tag{1}$$

$$D_w = \frac{\sum\limits_{i=1}^{N} n_i D_i^2}{\sum\limits_{i=1}^{N} n_i D_i} \tag{2}$$

$$D_v = \frac{\sum\limits_{i=1}^{N} n_i D_i^4}{\sum\limits_{i=1}^{N} n_i D_i^3} \tag{3}$$

The cuts were taken from the core of bars perpendicular to the flow direction. As a rough approximation, the particles were assumed to be "perfectly spherical" in the calculations.

Fracture surfaces were observed by scanning electron microscopy (SEM) at accaleration voltages of about 5–10 kV on gold-coated surfaces.

Mechanical tests

Mechanical tests were performed on injection molded specimens of $80 \times 10 \times 4$ mm^3. All the materials were molded under the same conditions; the MFR of the samples was not affected by molding. The parts were not annealing or conditionned in any way prior testing. Low speed bending tests were conducted according to DIN 53452/57 with a crosshead speed of 5 mm/min, and notched Charpy impact tests at 3.8 m/s according to ISO 179-2/1eA.

The ductile–brittle transitions were carried out on an instrumented Charpy device (Roell Amsler RKP 50, instrumented by HKE) with 50 J pendulum and a test speed of 1.5 m/s using SENB (single etched notched bending) specimens ($a/W = 0.25$) following ISO 179. A rough screening in steps of 10 K was performed between −60 and 100°C to get a first idea of the temperature associated with the ductile–brittle transition. It was followed by a fine screening in steps of 2 K around this transition temperature. For data acquisition and data reduction a software developed in Linz at Borealis was used.

Force-displacement curves were recorded and analyzed. The work to break, G_{tot}, was calculated from

$$G_{tot} = \frac{U_{tot}}{B(W - a)} \tag{4}$$

where U_{tot} is the energy to break of the SENB specimen, B the thickness of the sample, W the width of the sample, and a the crack length.

The indicated G_{tot} values in the ductile range have to be considered with caution. Since the samples did not break, only the broken sample width, W_{broken}, involved in the fracture process ($W_{broken} < W$) should have been taken in account in calculations. The G_{tot} are thus underestimated increasingly as the test temperature increased (W_{broken} decreasing with increasing temperature).
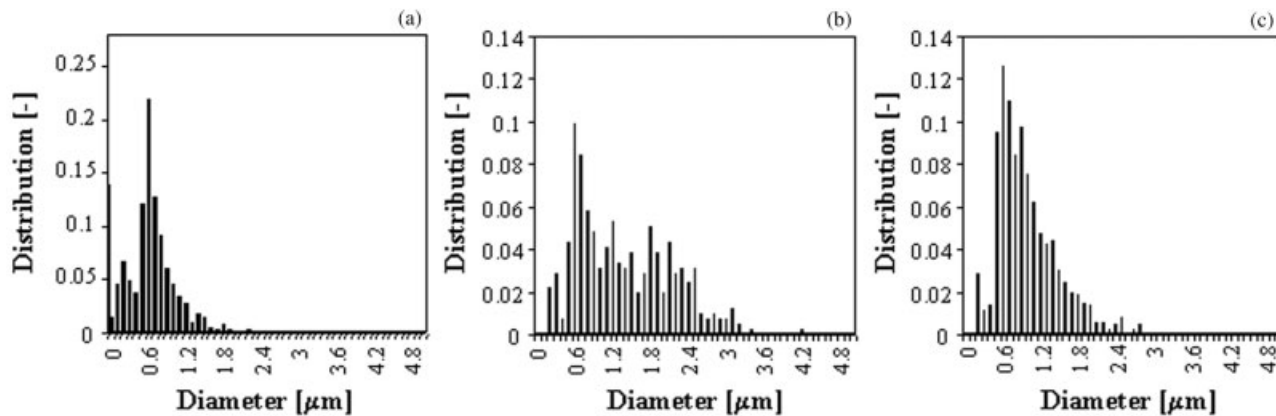
Figure 2 Particle size distribution in number of M-1.7, M-3, and M-6. Pay attention to the changes in scale between M-1.7 and M-3, M-6.

RESULTS AND DISCUSSION

Morphology

The morphology of the iPP/EPR blends varied with the rubber IV. The smallest particles were observed with the lowest IV as shown in the micrographs (Fig. 1) and illustrated by their particle size distribution in number (Fig. 2). With increasing IV, they coarsened; numerical data are reported in Table II. A wide maximum in D_n was observed at between IV = 2.7 to 4.7 dL/g. Its decrease for M-6.0, illustrated in Figure 3, is supported by theoretical considerations.[5]

The morphology of the blends is indeed strongly related to the ratio, μ, of the viscosities of the dispersed phase, η_b, and continuous phase, η_m. It actually controls the rate of phase separation by coalescence and distribution of mechanical work during processing. All other parameters being kept constant, a rather fine dispersion is expected in case of

1. a high molecular weight of the rubber compared to the matrix because a reduced flowability of the minor phase decreases the rate of agglomeration of large particles;
2. a low molecular weight of the rubber compared to the matrix: though the rate of agglomeration is faster, the mechanical deformation of the dis-

persed phase is stronger and thus enhances breakup of coalesced particles.

A maximum in the particle size of the dispersed phase is therefore expected for intermediate rubber molecular weights. However, little experimental evidence was observed for iPP/EPR or iPP/EPDM blends up to now, most of the studies reporting an increase of the particle size with increasing IV,[12,30,32–40] except refs. 5 and 41. An attempt to get an order of magnitude for the viscosity ratios of our materials was made using data from the literature, assuming the shear-rate developing during mixing in the extruder to be 100 rad s^{-1}. Indeed, since the polymerization takes place in a two-stage process, the second component (EPR) was not accessible independently. Input data taken from ref. 42 for a plate–plate geometry at 190°C are presented in Table III, calculations for the viscosities, η^*, for our grades in Table IV, assuming linear correlations between viscosities and M_w over the whole investigated ranges. The viscosity ratios, μ, are given in Table V; the values indicated for a rubber composition

TABLE II
Average Particle Size in Number, D_n, in Weight, D_w, and in Volume, D_v, of the Investigated Materials

	D_n (μm)	D_w (μm)	D_v (μm)
M-1.7	0.74	0.93	1.42
M-2.1	1.07	1.57	2.84
M-2.7	1.41	1.96	2.74
M-3.0	1.41	1.82	2.38
M-3.9	1.37	1.77	2.61
M-4.7	1.32	1.67	2.38
M-6.0	1.04	1.29	1.88
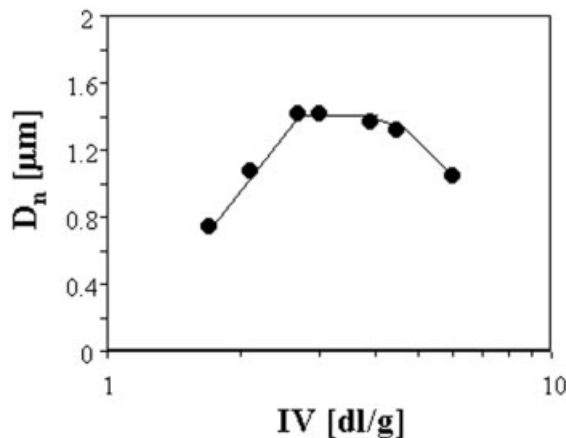
Figure 3 Average particle size, D_n, plotted vs. the logarithm of the intrinsic viscosity (IV) of the rubbery phase.

TABLE III
Input Data Taken for Calculations in TABLE III from Ref. 42.

	MFR Matrix (g/10 min)	M_w (g/mol)	$C_2/(C_2 + C_3)$ [wt %]	η^* [Pa s]
PP-1	60	215,000	—	120
PP-2	12	375,000	—	330
EPR-1	—	361,000	60	2,300
EPR-2	—	708,000	60	4,300
EPR-3	—	810,000	60	5,300
EPR-4	—	1,017,000	60	7,000
EPR-5	—	695,000	40	3,000

The η^* was measured on $\eta^* = f(\omega)$ plots at $\omega = 100$ rad/s. $C_2/(C_2+C_3)$ represents the ethylene proportion in the rubber.

TABLE V
Evaluation of μ at $\omega = 100$ rad/s for M-1.7 to M-6.0

|	μ_{60} (L)	μ_{40} (L)
M-1.7	5.1	3.5[a]
M-2.1	7.6	5.3[a]
M-2.7	10.3	7.2[a]
M-3.0	13.8	9.6[a]
M-3.9	14.0	13.2[a]
M-4.7	20.1	14.0[a]
M-6.0	33.5	23.3[a]

The μ_{60} values are directly extracted from Table III, valuable for a $C_2/(C_2+C_3) = 60$ wt %.

[a] The μ_{40} values are extrapolated from the μ_{60} one using the ratio η^*(EPR-5)/η^*(EPR-2) indicated in Table II. They are valuable for an EPR composition having 40% in weight of ethylene.

with 40 wt % of ethylene are those that reflect the closest the reactor-made particles. They varied roughly linearly with the IV of the rubber following $\mu = 4.3 * \text{IV(EPR)} - 4$, exhibiting values at between 3 and 25. These μ are about 2–10 times higher than the values reported (or evaluated) in (from) other publications. This fact might explain why the decrease of the particle size with sufficiently high M_w (and high matrix MFR!) has not often been highlighted before.

Besides, the evaluations of D_w and D_v gave accurate indications about the particle size distributions, which confirmed visual observations on both TEM and SEM micrographs. For M-2.1 and M-2.7, they were rather broad, with particles ranging from 0.2 to 5 μm. With increasing IV, they became narrower; particles of more than 2.5–3 μm disappeared almost completely, leading to lower average particle sizes in weight and in volume.

Mechanics—standard static properties

Static properties were only little influenced by the rubber IV with a yield stress of about 25.6 ± 0.4 MPa and a Young modulus of about 1030 ± 30 MPa, suggesting them to be controlled by the iPP matrix. The focus is thus be set on impact properties.

TABLE IV
Evaluation of η^* at $\omega = 100$ rad/s for EPR-IV = 1.7 to EPR-IV = 1.7 Using the Linear Correlation Between η^* and M_w of EPR-1, EPR-2, EPR-3, and EPR-4[42]

	MFR Matrix (g/10 min)	M_n (g/mol)	η^* (Pa s)
PP	40	260,000	240
EPR - IV = 1.7	—	233,000	1,230
EPR - IV = 2.1	—	320,000	1,850
EPR - IV = 2.7	—	412,000	2,500
EPR - IV = 3.0	—	530,000	3,350
EPR - IV = 3.9	—	706,000	4,600
EPR - IV = 4.7	—	745,000	4,875
EPR - IV = 6.0	—	1,200,000	8,110

Mechanics—standard dynamic properties

Specimens were tested at 23 and −20°C using a Charpy noninstrumented device. They all broke in a brittle manner. At room temperature, the energy to break, G_{break}, decreased linearly with the logarithm of the total MFR ranging from 12.9 kJ/m^2 for MFR = 10 to 4.5 kJ/m^2 for MFR = 26 g/10 min as shown in Figure 4. A convenient way to get the influence of the IV of the rubber was to plot it toward G_{break}. As illustrated in Figure 5, the impact energies increased linearly with the logarithm of the IV of the EPR. Although such linear correlations were much less pronounced at lower temperature, the same global evolutions were observed at −20°C.

These results could be attributed either directly to the higher molecular weight of the rubber or to the morphological changes induced by varying the IV of the particles. To solve this ambiguity ductile–brittle transitions of M-1.7, M-3, and M-6 were determined.
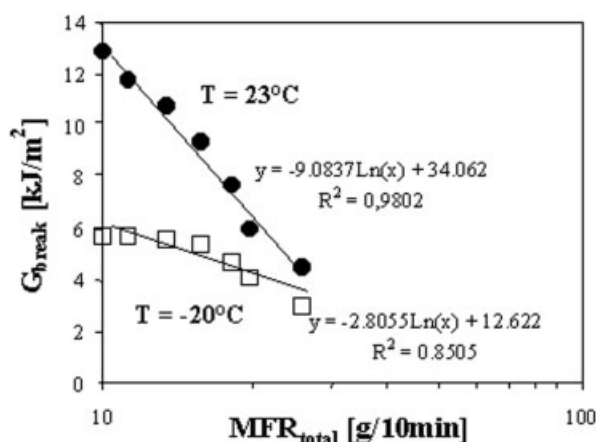
Figure 4 Standard notched Charpy fracture energy, G_{break}, plotted against the logarithm of the total MFR at −20 and 23°C.
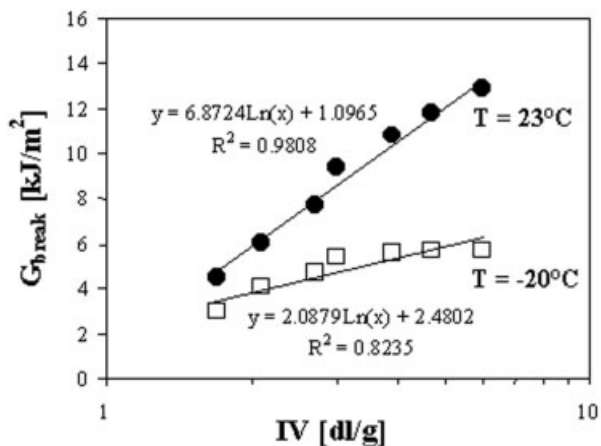
Figure 5 Standard notched Charpy fracture energy, G_{break}, plotted against the logarithm of the intrinsic viscosity of the particles at −20 and 23°C.

Mechanics: ductile–brittle transition

The determination of the ductile–brittle transition is the method of choice for apprehending the fracture properties of polymers,[9–12,16,23,43–48] since it takes into account their time–temperature dependent behavior. To get it, speed can be varied over several decades while keeping the temperature constant, or a wide range of temperature can be scanned in controlled steps at given impact velocity. In the first case, the higher the speed at which the tough-to-brittle transition occurs, the better the material in terms of resistance to fracture. In the second case, the lower the temperature at which the brittle-to-ductile transition occurs, the better the material. In this study, temperature was varied between −60 and 100°C. Typical force-displacement ($F − d$) curves are reported in Figure 6; their associated fractured surfaces in Figure 7.

It is, however, always challenging to determine an indisputable ductile-to-brittle transition, since with increasing temperature (decreasing speed!), four material behaviors are observed (and thus three successive transitions occur!):

- A brittle behavior characterized by a linear elastic force-displacement ($F − d$) curve. It was not observed with the investigated materials.
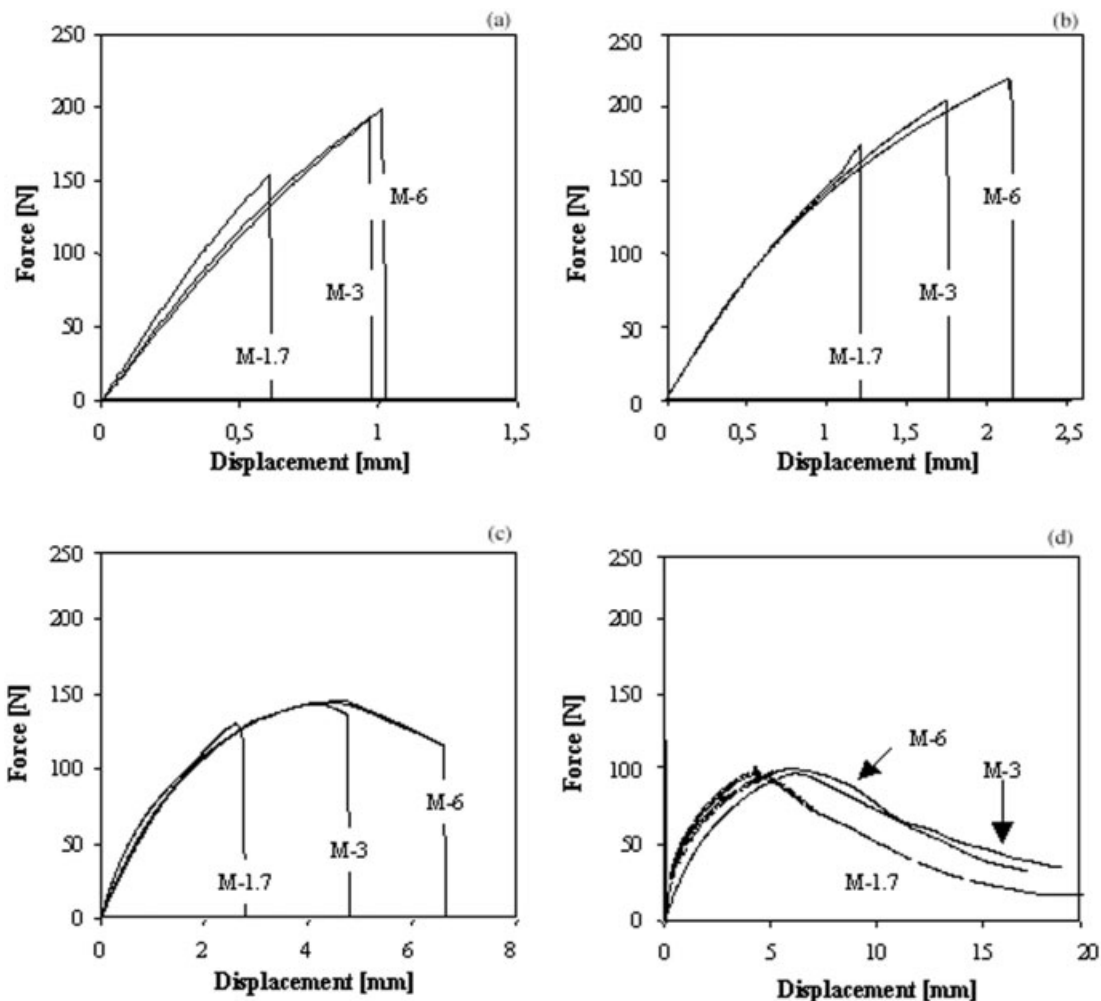
Figure 6 Typical force-displacement curves at (a) 50°C, (b) 0°C, (c) 40°C, and (d) 70°C for M-1.7, M-3, and M-6.
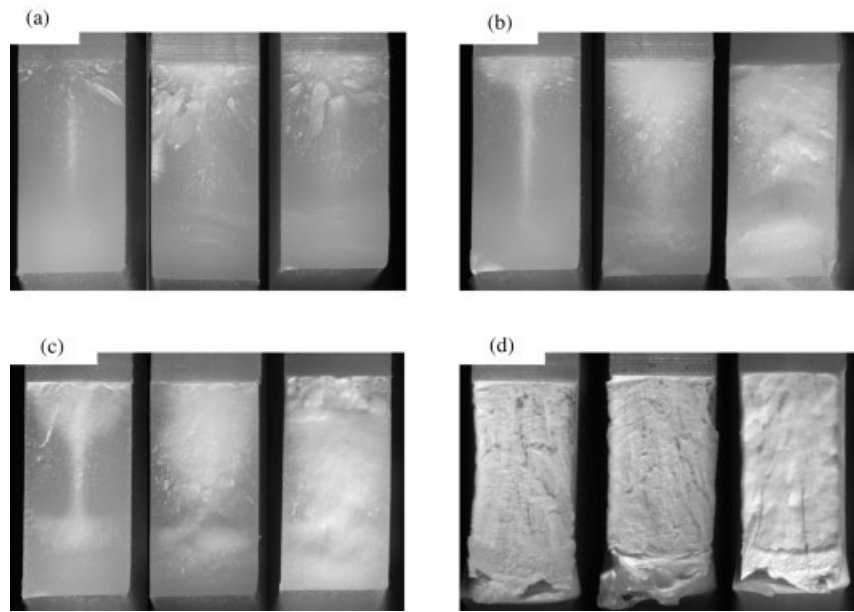
Figure 7 Typical fracture surfaces at (a) −50°C, (b) 0°C, (c) 40°C, and (d) 70°C for M-1.7, M-3, and M-6 (from left to right). Optical microscopy.

- A semibrittle behavior [Fig. 6(a) and (b)] with pronounced nonlinearity prior to unstable crack propagation. Fracture occurred before the critical stress to flow (yield stress) could be reached. The fracture surfaces were very rough, composed of several planes of macrocracks (the size of which decreased with increasing temperature). Stress-whitening, accounting for changes in the refractive index of the material (and thus to voiding in form of matrix crazing or particle cavitation), was not visible.
- A semiductile behavior [Fig. 6(c)] with initiation and partial development of the damage mechanisms before unstable fracture. The fracture surface was whitened in an extent which increased with increasing temperature;

- A ductile behavior [Fig. 6(d)] characterized by stable crack propagation and an entire stress-whitened fracture surface. Specimens did not break.

Although the semiductile to ductile transition is known to be geometry dependent, it was the one we worked with because (1) the huge energy gap associated with it made its determination easy and (2) was of practical relevance.

In Figure 8, the evolution of the total energy dissipated by the specimen, G_{tot}, is plotted against the temperature. The ductile–brittle transitions highlighted by arrows taken to be the inflexion points of
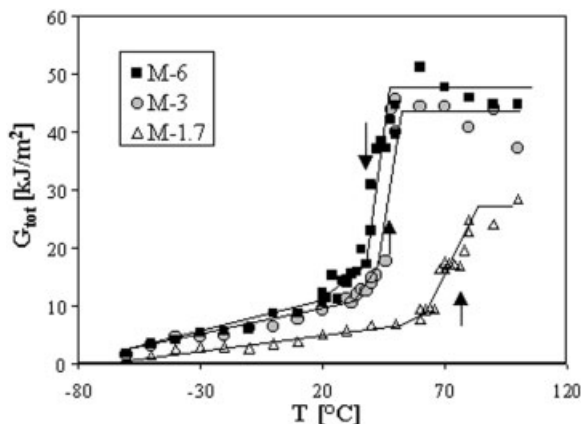
Figure 8 Energy to break, G_{tot}, plotted against the temperature for M-1.7, M-3, and M-6. The arrows indicated the temperature at which the ductile–brittle transition occurred.
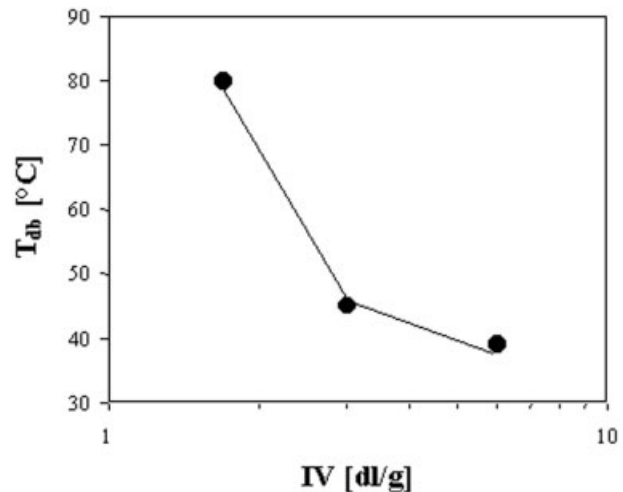
Figure 9 Temperatures at which the ductile–brittle transition occur plotted over the logarithm of the IV of the EPR phase.
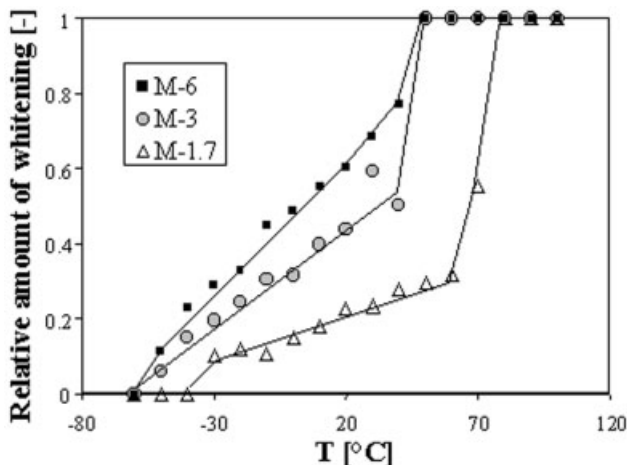
Figure 10 Amount of stress-whitening on the fracture surfaces plotted against temperature for M-1.7, M-3, and M-6.

the curves are about 80°C for M-1.7, 45°C for M-3, and 39°C for M-6: the higher the IV the lower its ductile–brittle transitions, T_{db} (i.e., the tougher the iPP/EPR blend). However, there was no linear correlation between the intrinsic viscosities of the rubber phase and the temperatures at which the T_{db} occur (Fig. 9), suggesting these latter to be mainly controlled by the particle morphology.

Moreover, as expected by definition of T_{db}, the ductile–brittle transition correlated rather well with the amount of stress-whitening developed at the front of the crack tip (Fig. 10). Besides a more precise investigation of the temperature range at between −30 and 40°C, domain in which all the materials were semiductile, showed a remarkable correlation between the extent of stress-whitening and the fracture energy of the specimens (Fig. 11).

Fractographic observations of the broken surfaces provided some additional information about the deformation mechanisms of the investigated materials, which all behaved in the same way (Fig. 12). At the

microscopic level, substantial changes could not be found between semibrittle and semiductile behaviors. In both cases, particles were pulled up from the surface, whereas the continuous phase seemed to be globally intact around them. This suggests that the particle could not act as stress concentrators and transmit the impact energy to the matrix. It remains unclear, however, if this is due to (1) a lack of cavitation of the rubber or (2) to the incapacity of the matrix to absorb the energy through craze formation, both propositions involving dilatational processes (leading to stress-whitening). Adhesion of the rubber to the matrix is actually also important but we assume it is very good in this case. Since in the semiductile regime, the fracture energy is proportional to the logarithm of the IV under unstable crack propagation (Fig. 13), we tend to (2). TEM investigations, however, would be useful to confirm it. Important modifications were only observed when the materials were ductile, and plasticity was extensive. Fracture of the blend occurred after significant elongation of sheared matrix ligaments.

Dynamical mechanical analysis

Despite being often underused, DMA is a precious tool for material characterisation.[23,49–54] The elastic modulus, G' (Fig. 14), was rather independent of the intrinsic viscosity of the dispersed phase, suggesting the loss factor, tan δ, to be governed by the loss modulus, G''. As obvious in Figure 15, the glass transition temperature, T_g, taken to be the maximum of tan δ, was about 0°C for the iPP matrix and about −50°C for the dispersed phase. A clear shift to higher temperatures of the T_g of the rubber was observed with increasing EPR intrinsic viscosity, considering either the maximum of tan δ or that of G'' (Fig. 16). Since the investigated blends did not exhibit a monotonic increase of the particle size with IV, this latter does not reflect the final morphology of the rubbery phase. It
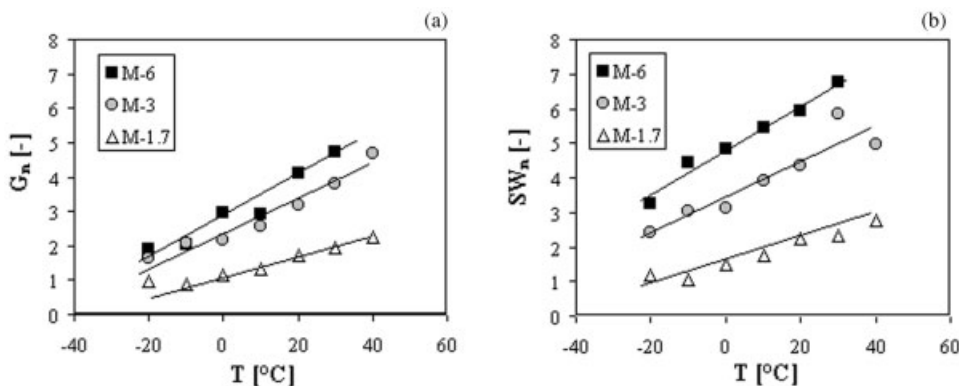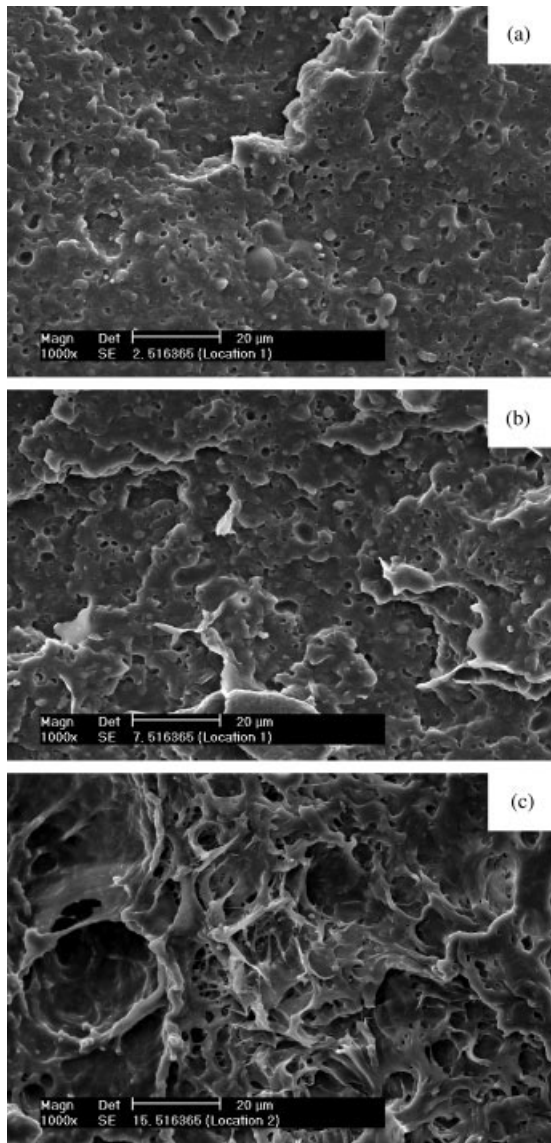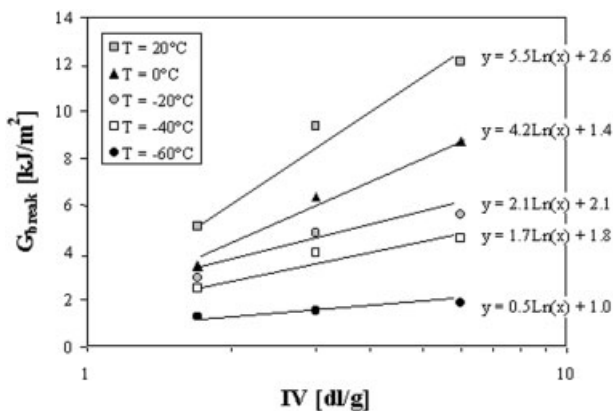

Figure 11 Correlation between notched impact energy and stress-whitening for macroscopic semiductile behaviors: (a) normalized energy to break (reference: energy to break of M-1.7 at −30°C); (b) normalized amount of stress-whitening (reference: amount of stress-whitening of M-1.7 at −30°C).
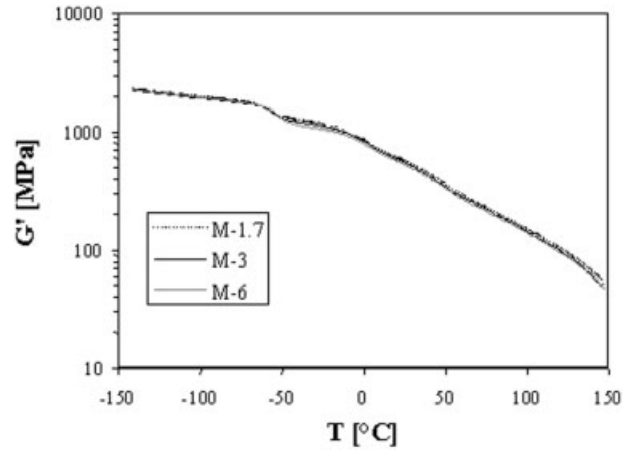
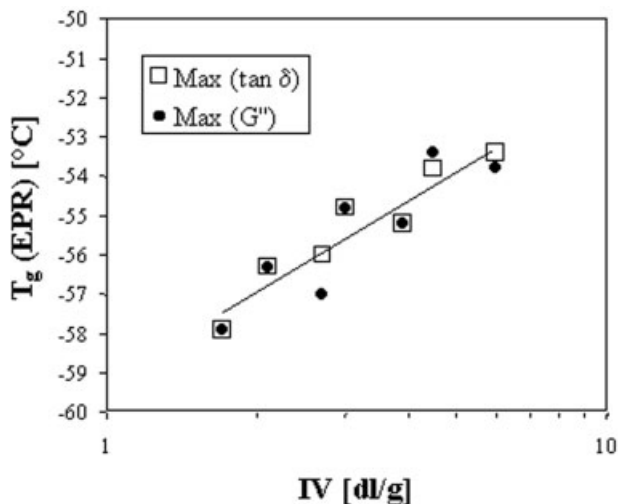**Figure 12** Fracture surfaces at (a) −50°C, (b) −0°C and (c) 70°C for M-6 observed by SEM.

Figure 14 Elastic modulus, G', plotted against the temperature for M-1.7, M-3, and M-6.

only suggests a low molecular weight rubber to be mobile before a more higher one. A rapid way to anticipate the fracture properties of the studied materials was to evaluate the strengths of the EPR relaxations, since they are direct indicators of the damping behavior of any given material and are thus expected to dominate its mechanical behavior at high loading rates. Figure 17 shows the areas under the EPR tan δ peak and PP tan δ peak as a function of the logarithm of the rubber IV. The data were normalized considering the area of the rubbery phase of M-1.7 to be equal to 1. From the observed linear positive correlation, a strong improvement of the impact properties was expected with increasing IV. It was indeed the case in the semiductile range, exemplified in Figure 18 for −20 and 23°C. Higher amounts of molecular entanglements in the amorphous rubber and tie-molecules between the crystalline parts might be responsible for the higher energy absorption with higher molecular weight of the dispersed phase. However, the number of rubber molecular relaxations did not correlate lin-

Figure 13 Notched impact strength, G_{break}, plotted against the logarithm of the IV of the rubber at between −60 and 20°C.
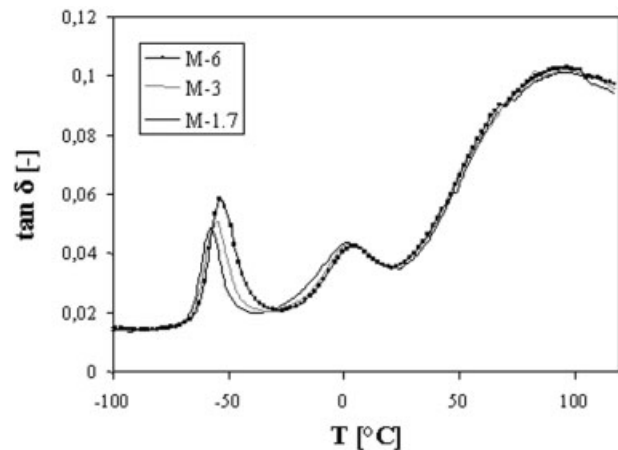
**Figure 15** Loss factor, tan δ, plotted against the temperature for M-1.7, M-3, and M-6.

Figure 16 Glass transition temperature, T_g, of the rubbery phase plotted against the logarithm of the intrinsic viscosity of the particles.

early with the temperature at which the ductile–brittle transition occurred (although providing the right material ranking), suggesting these molecular motions do not reflect the particle size changes, which were induced by varying the rubber molecular weight. A detailed report about the use of DMA for estimating toughness will be published latter.

CONCLUSION

The influence of the rubber molecular weight on the impact properties of seven iPP/EPR reactor blends was investigated by varying the EPR intrinsic viscosity from 1.7 to 6 dL/g. The induced changes in the morphology were explained by the competition be-
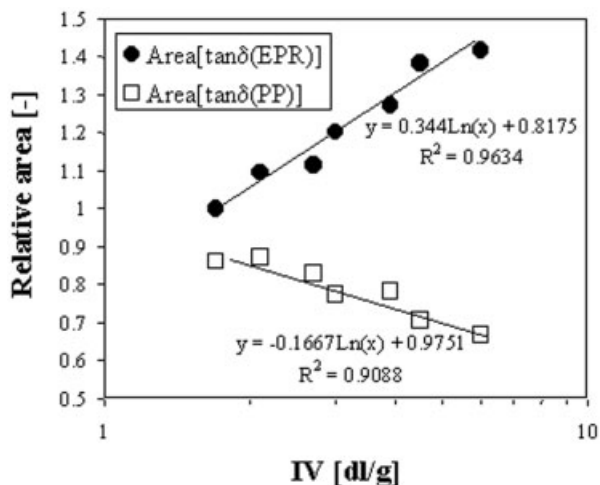
Figure 17 Normalised areas under the EPR tan δ and PP tan δ peaks plotted against the logarithm of the intrinsic viscosity of the particles. The area under the EPR tan δ peak of M-1.7 was chosen as reference.
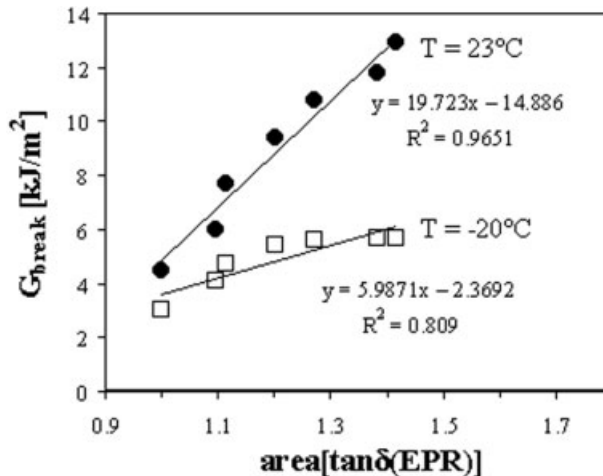
Figure 18 Evolution of the area under the EPR tan δ peak against the standard notched Charpy fracture energy, G_{break}, for the investigated materials.

tween coalescence and breakup of particles during processing, and rationalized in terms of viscosity ratios between dispersed phase and matrix.

A linear increase of toughness was observed with increasing the intrinsic viscosity of the EPR particles on a logarithmic scale in standard Charpy tests carried out at −20 and 23°C. These measurements, however, were insufficient to assess for the parameter that controlled the mode of fracture of the grades: either the M_w of the rubber or the average particle size of the dispersed phase. A screening in between −60 to 100°C at fixed test speed showed this latter to be of major importance. However, despite decreasing with increasing rubbery IV, the temperature at which the ductile–brittle transitions occurred correlated not *linearly* with the logarithm of the intrinsic viscosity of the rubber.

The strength of molecular relaxations associated with the rubbery phase, estimated by DMA, reflected therefore only qualitatively the macroscopic behavior of the blend. Moreover, under unstable crack the amount of stress-whitening that develops at the fracture surfaces correlated strongly with the energy to break of the materials suggested the matrix to be the limiting factor in the deformation mechanisms of the investigated materials.

References

1. Perkins, W. G. Polym Eng Sci 1999, 39(12), 2445.
2. Lear, P. L.; Tucker, D.; Lee, S. Rev Proc Chem Eng 1999, 2, 277.

3. Galli, P.; Haylock, J. C.; Simonazzi, T. In Polypropylene. Structure, Blends and Composites; Karger-Kocsis, J., Ed.; Chapman & Hall: London, 1995; pp. 1–24.

4. Liebermann, R. B.; Le Noir, R. T. In Polypropylene Handbook; Moore, E. D., Carl Hanser Verlag: Munich, 1996; pp. 287–301.

5. van der Ven, S. Polypropylene and Other Polyolefins: Polymerisation and Characterization; Studies in Polymer Science 7; Elsevier Science Publishers BV: Amsterdam, 1990; chap 6, pp. 289–336.

6. Bernreitner, K; Hammerschmid, K. In Polypropylene: An A-Z Reference; Karger-Kocsis, J., Ed.; Kluivert Publishers: Dordrecht, 1999; pp. 149–157.

7. Gahleitner, M.; Wolfschwenger, J.; Bachner, C.; Bernreitner, K.; Neiβl, W. J Appl Polym Sci 1996, 61, 649.

8. Jang, B. Z.; Uhlmann, D. R.; Van der Sande, H. J Appl Polym Sci 1985, 30, 2485.

9. Van der Wal, A.; Nijhof, R.; Gaymans R. J. Polymer 1998, 39(26), 6781.

10. Van der Wal, A.; Nijhof, R.; Gaymans, R. J. Polymer 1999, 40, 6031.

11. Van Der Wal, A.; Gaymans, R. J. Polymer 1999, 40, 6045.

12. Van der Wal, A.; Verheul, A. J. J.; Gaymans, R. J. Polymer 1999, 40, 6057.

13. Tjong, S. C.; Li, W. D.; Li, K. Y. Polym Bull 1997, 38, 721.

14. Dwyer, S. M.; Boutni, O. M.; Shu C. In Polypropylene Handbook; Moore, E. P., Ed.; Carl Hanser Verlag: München, 1996; pp. 211–235.

15. Karger-Kocsis, J.; Kulesnev, V. N. Polymer 1982, 23, 699.

16. Van der Wal, A.; Mulder, J. J.; Thijs, H. A.; Gaymans, R. J. Polymer 1998, 39(22), 5467.

17. Sugimoto, M.; Ishikawa, M.; Hatada, K. Polymer 1995, 36, 19, 3675.

18. Greco, R.; Ragosta, G. J Mater Sci 1988, 23, 4171.

19. Fukahara, N. Polym Testing 1999, 18, 135.

20. Zhang, X. C.; Butler, M. F.; Cameron, R. E. Polymer 1999, 41, 3797.

21. Van der Wal A.; Mulder, J. J.; Gaymans, R. J. Polymer 1998, 39(22), 5477.

22. Karger-Kocsis, J. Polym Bull 1996, 36, 117.

23. Grein, C.; Béguelin, P.; Plummer, C. J. G.; Kausch, H.-H.; Tézé, L.; Germain, Y. In Fracture of Polymers, Composites and Adhesives; Williams, J. G., Pavan, A., Eds. ESIS Publication 27; Elsevier Science: Oxford, UK, 2000, pp. 319–333.

24. Jancar, J.; Di Anselmo, A.; Di Benedetto, A. T.; Kucera, J. Polymer 1993, 34(8), 1684.

25. Chou, C. J.; Vijayan, K.; Kirby, D.; Hiltner, A.; Baer, E. J Mater Sci 1988, 23, 2521.

26. Chou, C. J.; Vijayan, K.; Kirby, D.; Hiltner, A.; Baer, E. J Mater Sci 1988, 23, 2533.

27. Grellmann, W.; Seidler, S.; Jung, K.; Kotter, I. J Appl Polym Sci 2001, 79, 2317.

28. Ramsteiner, F. Acta Polym 1991, 42(11), 584.

29. D'Orazio, L.; Mancarella, C.; Martuscelli, E.; Sticotti, G.; Cecchin, G. J Appl Polym Sci 1999, 72, 701.

30. D'Orazio, L.; Mancarella, C.; Martuscelli, E.; Polato, F. Polymer 1991, 32(6), 1186.

31. Irani, R. R.; Callis, C. F.; Particle Size: Measurement, Interpretation and Application; John Wiley & Sons: New York, 1963.

32. Premphet, K; Paecharoenchai, W. J Appl Polym Sci 2001, 82, 2140.

33. Naiki, M.; Matsumura, T.; Matsuda, M. J Appl Polym Sci 2002, 83, 46.

34. Paulik, C. E.; Neiβl, W. Annu Tech Conf—Soc Plast Eng 1998, 56th (Vol 2), 2565.

35. D'Orazio, L.; Mancarella, C.; Martuscelli, E.; Sticotti, G. J Mater Sci 1991, 26, 4033.

36. Karger-Kocsis, J.; Kallo, A: Kuleznev, N. Polymer 1984, 25, 279.

37. D'Orazio, L.; Cecchin, G. Polymer 2001, 42, 2684.

38. Gemmati, M.; Nazokdast, H.; Shariat Panahi, H. J Appl Polym Sci 2001, 82, 1129.

39. Kim, B. K.; Do, I. H. J Appl Polym Sci 1996, 61, 439.

40. D'Orazio, L.; Mancarella, C.; Martuscelli, E.; Sticotti, G.; Massari, P. Polymer 1993, 34, 17, 3671.

41. Everaert, V.; Aerts L.; Groeninckx, G. Polymer 1999, 40, 6627.

42. Migri, F.; Huneault, M. A.; Ajji A.; Ko, G. H.; Watanabe F. J Appl Polym Sci 2001, 82, 2113.

43. Gensler, R.; Plummer, C. J. G.; Grein, C.; Kausch, H.-H.; Polymer 2000, 41, 3809.

44. Béguelin, P.; Kausch, H.-H. J Phys, IV France 1997, 933.

45. Gaymans, R. J. In Polymer Blends. Paul, D. R., Bucknall, C. B. Eds.; New York, 2000; pp. 177–224.

46. Starke, J. U.; Michler, G. H.; Grellmann, W.; Seidler, S.; Gahleitner, M.; Fiebig, J.; Nezbedova, E. Polymer 1998, 39, 1, 75–82.

47. Béguelin, P.; Kausch, H. H. In Impact and Dynamic Fracture of Polymers and Composites; Williams, J. G., Pavan, A., Eds.; Mechanical Engineering Publications: London, 1995; pp. 3–19.

48. Julien, O.; Béguelin, P.; Monnerie, L.; Kausch, H.-H. In ACS Advances in Chemistry Series No. 252, Toughened Plastics II, Novel Appproaches in Science and Engineering; Riew, C. K., Kinloch, A. J., Eds.; American Chemical Society: Washington, DC, 1996. pp. 233–249.

49. Ramsteiner, F. Kunststoffe 1983, 72(3), 148.

50. Karger-Kocsis, J.; Kuleznev, V. N. Polymer 1982, 23, 699.

51. Karger-Kocsis, J.; Kiss, L. Polym Eng Sci 1987, 27(4), 254.

52. Vincent, P. I. Polymer 1974, 15, 111.

53. Kisbenyi, M.; Birch, M. W.; Hodgkinson, J. M.; Williams, J. G. Polymer 1979, 20, 1289.

54. Woo, L.; Westphal, S.; Ling, M. T. K. Polym Eng Sci 1994, 34(5), 420.